A Hybrid Vibration Reduction Strategy for Mistuned Blisks Using Intentional Mistuning of Hard-Coating Damping

Feng Gao

School of Automation, Wuxi University, Wuxi 214105, P.R. China. E-mail: fenggao@cwxu.edu.cn

Jingjun Li

School of Mechanical Engineering and Automation, Northeastern University, Shenyang 110819, P.R. China.

(Received 1 February 2026; accepted 8 May 2026)

To ensure the working performance of mistuned blisks, a hybrid vibration reduction strategy using the material damping and intentional mistuning capacities induced by the hard coating was proposed here. For solving vibration characteristics of mistuned blisks deposited hard coating efficiently, a novel reduced-order model was established using the improved component modeling method with dual reduction of degrees of freedoms (DOFs) firstly, and then validated by comparing the simulation results from the testing. Next, by the material damping capacity of the uniform-thickness hard coating, the passive vibration reduction strategy for mistuned blisks was investigated, and the specific influence of hard coating on vibration characteristics of mistuned blisks was discussed for the selection of intentional mistuning pattern. Finally, the small intentional stiffness and damping mistuning capacities were constructed by various coating thicknesses of different sectors, and then the hybrid vibration reduction analysis for mistuned blisks, which utilizes the material damping capacity and the small intentional mistuning induced by hard coating simultaneously, was further investigated for strategy validation.

NOMENCLATURE

blisks	integrally bladed disks
DOFs	degrees of freedoms
HC	hard coating
DHC	HC mistuned blisks with dual mistuning
FEM	finite element model
ROM	reduce-order model

1. INTRODUCTION

Integrally bladed disks (blisks) were used widely in advanced aero-engines due to their simplified mechanical structure and superior aerodynamic performance.[1] In an ideal case, the blisks were always designed as the tuned structure with identical sectors. In fact, due to manufacture errors, wear during service and other causes, some random deviations among the blades, called mistuning, occur inevitably, which always leads to the localization of vibration energy in certain sectors.[2] Meanwhile, the structural damping of blisks was relatively low due to the lack of friction damping originated from the dry friction of components such as tenons and mortises.[3] Thus, the mistuned blisks were more vulnerable to the high cycle fatigue in an adverse environment.[4] Therefore, the damping enhancement technologies for vibration reduction of the mistuned blisks need to be conducted necessarily.

Considering the integrated structural characteristic, the dry friction damping technology, such as under-platform damper,[5,6] commonly used in segmented bladed disks was very difficult to applied to the mistuned blisks. Thus, New damping technologies were proposed by some researchers for the vibration suppression of mistuned blisks, such as the piezoelectric shunt dampers,[7–10] the constrained layer dampers,[11,12] the absorbers array dampers,[13] and the hybrid flexible dampers with dry friction and piezoelectric.[14] However, these dampers cannot bear the high temperature and strong corrosion durably in the actual operating environment of engines. Moreover, the frictional ring dampers were modified and used to conduct vibration reduction,[14–16] which were very difficult in industrial applications because of the cumbersome implementation. In addition, an approach by the hard coating materials, which has been commonly used as the surface treatment for wear resistance, high-temperature resistance, anti-friction and anti-corrosion, with specific high damping capability were developed and the adopted to mistuned blisks, then the lumped-parametric model,[18,19] the continuous-parametric model[19,20] and the simplified finite element model[20–23] were established for vibration analysis of the realistic mistuned blisks with uniform hard coating, however the above-mentioned models can only be employed for the approximate qualitative analysis during the preliminary research, and cannot meet the accuracy requirements in engineering applications.

Theoretically, the full order finite element model (FEM) of realistic blisks, which has the large amount of DOFs, can be effectively adopted to obtain vibration characteristics of tuned blisks with identical sectors according to the cyclic symmetry characteristics. However, the actual solution process for the mistuned blisks was extremely time-consuming because of the mistuning characteristics. Therefore, the reduced order FEM was investigated firstly by Castanier,[24] and employed by some researchers to solve the vibration characteristics of mistuned blisks[25] and HC mistuned blisks[26–29] efficiently. How-

ever, these studies do not consider the hybrid vibration reduction method for realistic mistuned blisks, and the reduce-order model (ROM) of HC mistuned blisks with single reduction in these studies still retains a relatively high number of DOFs (about fifty to sixty percent of DOFs full order model), which bring about a prohibitively large computational cost in vibration reduction analysis of the realistic mistuned blisks by the intentional mistuning of hard coating, because the mistuning pattern and its value in each HC blade were different and always changes generated by adjusting coating thickness actively.

In this research, the hybrid vibration reduction analysis of mistuned blisks with small intentional mistuning, which was generated by the various coating thickness, was investigated using the improved component model. In Sec. 2, the ROM of HC mistuned blisks with dual DOFs reduction was established. The interface DOFs between the HC blade and the disk components were first reduced, then the retained interface DOFs were transformed into the internal DOFs of components; and the internal DOFs of components were reduced secondly by the free and fixed interface method, respectively. Finally, a ROM for HC mistuned blisks was established by modal synthesis. In Sec. 3, an actual blisks deposited NiCrAlY hard coating on mistuned blades was selected as benchmark case, and then the model validation was verified by comparing with the testing results in terms of the computational efficiency and calculation accuracy. Particularly, the passive vibration reduction strategy for mistuned blisks was developed using the material damping capacity of NiCrAlY hard coating, and the specific influence of hard coating on mistuned blisks was then studied; finally, the small intentional stiffness and damping mistuning were conducted by various coating thickness, and the hybrid vibration reduction strategy for the mistuned blisks, using the material damping capacity and the intentional mistuning simultaneously, was further investigated.

2. REDUCED-ORDER MODEL

2.1. The First Reduction for Interface DOFs

The full stage and sector solid model of mistuned blisks deposited hard coating damping on all blades was shown in Fig. 1(a). Its corresponding FEM were then established using the 3D SOLID185 elements, as shown in Fig. 1(b). In traditional component methods, the HC mistuned blisks can be decomposed into the HC blade and the disk components, and the whole interface DOFs between the HC blade and the disk components were taken into consideration for vibration analysis, nevertheless, this strategy exhibits negligible improvement in computational accuracy while significantly increasing the computational cost. Therefore, the aforementioned interface DOFs can be rationally reduced, and its reduction principle, specifically involving the dimensionality reduction of the interface mode set within the Ritz basis of the component method, was illustrated in Fig. 2. In which, on the premise that the reduced interface nodes can still fully represent the interface deformation, an efficient reduced-order model that accurately simulates the structural deformation was developed finally.

Taking the HC blade component as an example, the specific reduction process of interface DOFs was introduced. The motion equation without structural damping can be expressed as:

$$\begin{bmatrix} \boldsymbol{M}_{b,BB} & \boldsymbol{M}_{b,B\Gamma} \\ \boldsymbol{M}_{b,\Gamma B} & \boldsymbol{M}_{b,\Gamma\Gamma} \end{bmatrix} \begin{bmatrix} \ddot{\boldsymbol{X}}_{b,B} \\ \ddot{\boldsymbol{X}}_{b,\Gamma} \end{bmatrix} + \begin{bmatrix} \boldsymbol{K}_{b,BB} & \boldsymbol{K}_{b,B\Gamma} \\ \boldsymbol{K}_{b,\Gamma B} & \boldsymbol{K}_{b,\Gamma\Gamma} \end{bmatrix} \begin{bmatrix} \boldsymbol{X}_{b,B} \\ \boldsymbol{X}_{b,\Gamma} \end{bmatrix} = \begin{bmatrix} \boldsymbol{0} \\ \boldsymbol{F}_{b,\Gamma} \end{bmatrix}; \tag{1}$$

where subscript b denotes the HC blade component; subscript B denotes the internal DOFs of HC blade; subscript Γ denotes the interface DOFs; $\boldsymbol{K}_b$, $\boldsymbol{M}_b$, $\boldsymbol{F}_b$ and $\boldsymbol{X}_b$ were the stiffness, mass, interface force matrices and the displacement vector, respectively.

According to the proposed method,[29] the aforementioned interface DOFs were selected evenly and reduced by half, and the retained interface DOFs were transformed into internal DOFs of HC blade component by the transformation matrix $\bar{\boldsymbol{U}}_b$. It can be expressed as:

$$\begin{bmatrix} \boldsymbol{X}_{b,B} \\ \boldsymbol{X}_{b,\Gamma} \end{bmatrix} = \begin{bmatrix} \boldsymbol{X}_{b,B} \\ \bar{\boldsymbol{X}}_{b,\Gamma} \\ \boldsymbol{X}_{re,\Gamma} \end{bmatrix} = \begin{bmatrix} \boldsymbol{I} & \boldsymbol{0} & \boldsymbol{0} \\ \boldsymbol{0} & \boldsymbol{0} & \boldsymbol{I} \\ \boldsymbol{0} & \boldsymbol{I} & \boldsymbol{0} \end{bmatrix} \begin{bmatrix} \boldsymbol{X}_{b,B} \\ \boldsymbol{X}_{re,\Gamma} \\ \bar{\boldsymbol{X}}_{b,\Gamma} \end{bmatrix} = \bar{\boldsymbol{U}}_b \begin{bmatrix} \bar{\boldsymbol{X}}_{b,B} \\ \bar{\boldsymbol{X}}_{b,\Gamma} \end{bmatrix}. \tag{2}$$

In Eq. (2), the $\boldsymbol{X}_{b,\Gamma}$, $\bar{\boldsymbol{X}}_{\mathrm{b,B}}$ and $\bar{\boldsymbol{U}}_b$ were expressed as:

$$\boldsymbol{X}_{b,\Gamma} = \begin{bmatrix} \bar{\boldsymbol{X}}_{b,\Gamma} \\ \boldsymbol{X}_{re,\Gamma} \end{bmatrix}, \quad \bar{\boldsymbol{X}}_{b,B} = \begin{bmatrix} \boldsymbol{X}_{b,B} \\ \boldsymbol{X}_{re,\Gamma} \end{bmatrix}, \quad \bar{\boldsymbol{U}}_b = \begin{bmatrix} \boldsymbol{I} & \boldsymbol{0} & \boldsymbol{0} \\ \boldsymbol{0} & \boldsymbol{0} & \boldsymbol{I} \\ \boldsymbol{0} & \boldsymbol{I} & \boldsymbol{0} \end{bmatrix}; \tag{3}$$

where $\boldsymbol{X}_{\mathrm{b,B}}$ and $\bar{\boldsymbol{X}}_{\mathrm{b,B}}$ were the pre-transformation and post-transformation internal coordinates of HC blade, respectively; $\boldsymbol{X}_{b,\Gamma}$ and $\bar{\boldsymbol{X}}_{b,\Gamma}$ were the pre-transformation and post-transformation retained interface coordinates of HC blade, respectively; $\boldsymbol{X}_{\mathrm{re},\Gamma}$ denotes reduced interface DOFs coordinates of HC blade, and $\boldsymbol{I}$ denotes identity diagonal matrix.

It should be noted that the matrix dimensions remain unchanged before and after transformation. In the subsequent component reduction process, the internal DOFs were condensed for the calculation of master mode matrix. The retained interface DOFs were used to compute the constraint mode matrix. By substituting Eq. (2) into Eq. (1) and transforming the corresponding coordinate, we can obtain:

$$\begin{bmatrix} \bar{\boldsymbol{M}}_{b,BB} & \bar{\boldsymbol{M}}_{b,B\Gamma} \\ \bar{\boldsymbol{M}}_{b,\Gamma B} & \bar{\boldsymbol{M}}_{b,\Gamma\Gamma} \end{bmatrix} \begin{bmatrix} \ddot{\bar{\boldsymbol{X}}}_{b,B} \\ \ddot{\bar{\boldsymbol{X}}}_{b,\Gamma} \end{bmatrix} + \begin{bmatrix} \bar{\boldsymbol{K}}_{b,BB} & \bar{\boldsymbol{K}}_{b,B\Gamma} \\ \bar{\boldsymbol{K}}_{b,\Gamma B} & \bar{\boldsymbol{K}}_{b,\Gamma\Gamma} \end{bmatrix} \begin{bmatrix} \bar{\boldsymbol{X}}_{b,B} \\ \bar{\boldsymbol{X}}_{b,\Gamma} \end{bmatrix} = \begin{bmatrix} \boldsymbol{0} \\ \bar{\boldsymbol{F}}_{b,\Gamma} \end{bmatrix}; \tag{4}$$

where

$$\begin{cases} \begin{bmatrix} \bar{\boldsymbol{M}}_{b,BB} & \bar{\boldsymbol{M}}_{b,B\Gamma} \\ \bar{\boldsymbol{M}}_{b,\Gamma B} & \bar{\boldsymbol{M}}_{b,\Gamma\Gamma} \end{bmatrix} = (\bar{\boldsymbol{U}}_b)^{\mathrm{T}} \begin{bmatrix} \boldsymbol{M}_{b,BB} & \boldsymbol{M}_{b,B\Gamma} \\ \boldsymbol{M}_{b,\Gamma B} & \boldsymbol{M}_{b,\Gamma\Gamma} \end{bmatrix} \bar{\boldsymbol{U}}_b = (\bar{\boldsymbol{U}}_b)^{\mathrm{T}} \boldsymbol{M}_b \bar{\boldsymbol{U}}_b, \\ \begin{bmatrix} \bar{\boldsymbol{K}}_{b,BB} & \bar{\boldsymbol{K}}_{b,B\Gamma} \\ \bar{\boldsymbol{K}}_{b,\Gamma B} & \bar{\boldsymbol{K}}_{b,\Gamma\Gamma} \end{bmatrix} = (\bar{\boldsymbol{U}}_b)^{\mathrm{T}} \begin{bmatrix} \boldsymbol{K}_{b,BB} & \boldsymbol{K}_{b,B\Gamma} \\ \boldsymbol{K}_{b,\Gamma B} & \boldsymbol{K}_{b,\Gamma\Gamma} \end{bmatrix} \bar{\boldsymbol{U}}_b = (\bar{\boldsymbol{U}}_b)^{\mathrm{T}} \boldsymbol{K}_b \bar{\boldsymbol{U}}_b, \\ \begin{bmatrix} \boldsymbol{0} \\ \bar{\boldsymbol{F}}_{b,\Gamma} \end{bmatrix} = (\bar{\boldsymbol{U}}_b)^{\mathrm{T}} \begin{bmatrix} \boldsymbol{0} \\ \boldsymbol{F}_{b,\Gamma} \end{bmatrix}. \end{cases} \tag{5}$$

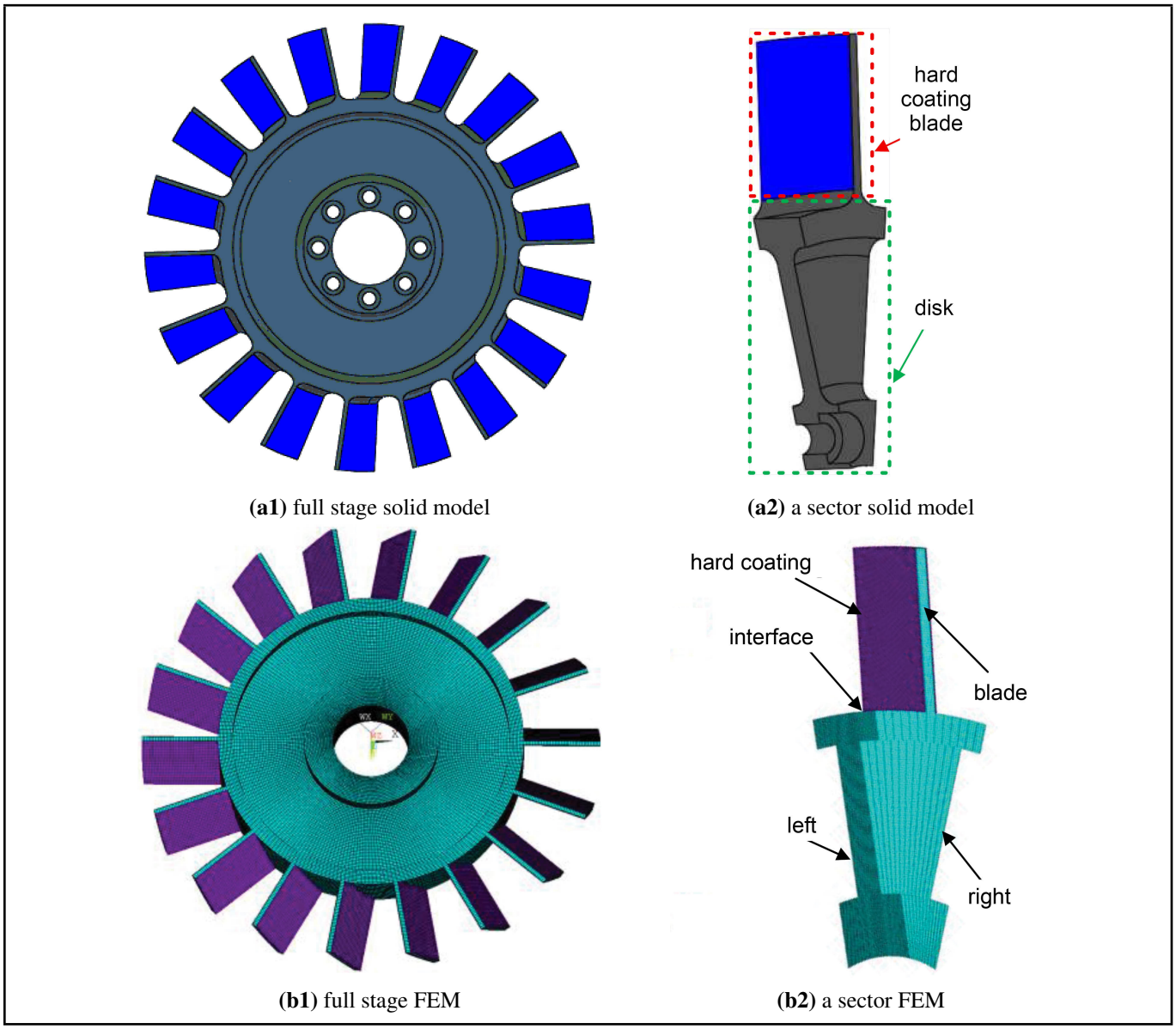

(a1) full stage solid model **(a2)** a sector solid model

(b1) full stage FEM **(b2)** a sector FEM

Figure 1. Full stage model and a sector model of mistuned blisks with HC blade.

and $\bar{\boldsymbol{M}}_b$, $\bar{\boldsymbol{K}}_b$, $\bar{\boldsymbol{F}}_b$ denote the stiffness, mass matrix, and interface force matrices of HC blade, respectively. Moreover, the transformation order of DOFs was analogous to the coordinate transformation sequence applied to displacements.

2.2. The Second Reduction for Component DOFs

In this section, the reduction for component DOFs was conducted by the improved component method. In which, the free-interface method was adopted for the interface treatment of the disk component, while the fixed-interface method was selected for that of each HC blade component. It should be noted that each component of HC mistuned blisks was reduced separately, and the specific procedure of component DOFs was illustrated in Fig. 3.

For the HC blade component, its internal DOFs can be condensed as follows. Using the reduced interface mass and stiffness matrices, the characteristics equation of HC blade component can be expressed as:

$$\left[\bar{\boldsymbol{K}}_{\mathrm{b,BB}} - \omega^2 \bar{\boldsymbol{M}}_{\mathrm{b,BB}}\right] \boldsymbol{\varphi}_b = \boldsymbol{0}. \tag{6}$$

The principal mode matrix of HC blade component $\boldsymbol{\Phi}_b$ was obtained as follows:

$$\boldsymbol{\Phi}_b = (\boldsymbol{\varphi}_{b,1}, \boldsymbol{\varphi}_{b,2}, \cdots, \boldsymbol{\varphi}_{b,n}); \tag{7}$$

and, using the solution method proposed by LI,[30] the constraint mode matrix of HC blade component $\boldsymbol{\Psi}_b$ can be obtained as:

$$\boldsymbol{\Psi}_b = -\bar{\boldsymbol{K}}_{b,\mathrm{BB}} \left(\bar{\boldsymbol{K}}_{b,\mathrm{B\Gamma}}\right)^T. \tag{8}$$

Subsequently, based on the Craig-Bampton component method, the modal matrix (i.e., the secondary reduced matrix) of HC blade component $\bar{\bar{\boldsymbol{U}}}_b$ can be derived as:

$$\bar{\bar{\boldsymbol{U}}}_b = \begin{bmatrix} \boldsymbol{\Phi_b} & \boldsymbol{\Psi_b} \\ \boldsymbol{0} & \boldsymbol{I} \end{bmatrix}. \tag{9}$$

Finally, the mass matrix $\bar{\bar{\boldsymbol{M}}}_b$ and the stiffness matrix $\bar{\bar{\boldsymbol{K}}}_b$ of HC blade component after secondary reduction were obtained and expressed as follows:

$$\bar{\bar{\boldsymbol{M}}}_b = (\bar{\bar{\boldsymbol{U}}}_b)^T \bar{\boldsymbol{M}}_b \bar{\bar{\boldsymbol{U}}}_b, \bar{\bar{\boldsymbol{K}}}_b = (\bar{\bar{\boldsymbol{U}}}_b)^T \bar{\boldsymbol{K}}_b \bar{\bar{\boldsymbol{U}}}_b; \tag{10}$$

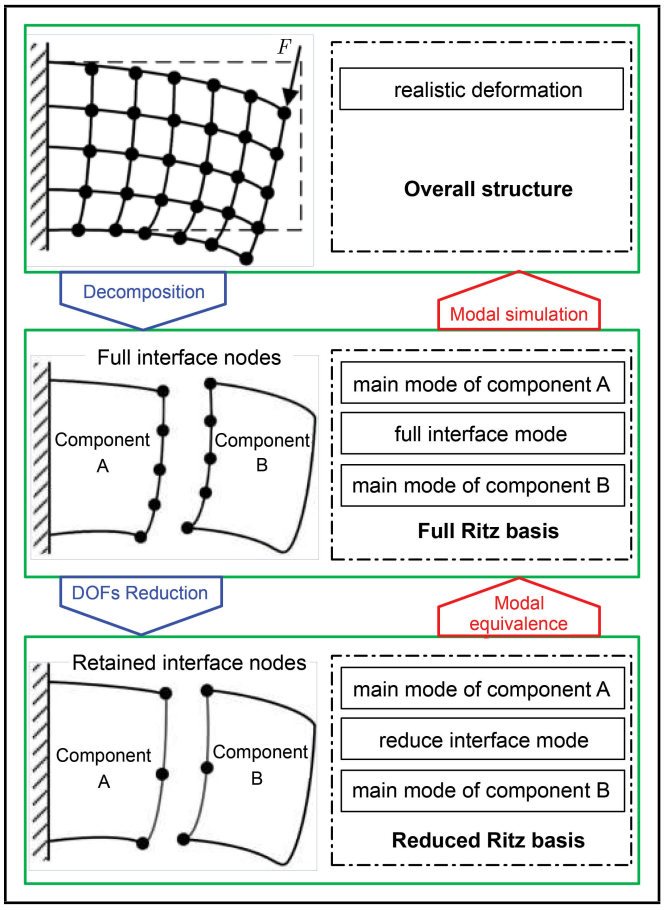

Figure 2. The first reduction principle of the interface DOFs.

$$\bar{\boldsymbol{M}}_b = \begin{bmatrix} \bar{\boldsymbol{M}}_{b,BB} & \bar{\boldsymbol{M}}_{b,B\Gamma} \\ \bar{\boldsymbol{M}}_{b,\Gamma B} & \bar{\boldsymbol{M}}_{b,\Gamma\Gamma} \end{bmatrix}, \quad \bar{\boldsymbol{K}}_b = \begin{bmatrix} \bar{\boldsymbol{K}}_{b,BB} & \bar{\boldsymbol{K}}_{b,B\Gamma} \\ \bar{\boldsymbol{K}}_{b,\Gamma B} & \bar{\boldsymbol{K}}_{b,\Gamma\Gamma} \end{bmatrix}. \tag{11}$$

For the disk component, the motion equation can be expressed as:

$$\begin{bmatrix} \bar{\boldsymbol{M}}_{d,BB} & \bar{\boldsymbol{M}}_{d,B\Gamma} \\ \bar{\boldsymbol{M}}_{d,\Gamma B} & \bar{\boldsymbol{M}}_{d,\Gamma\Gamma} \end{bmatrix} \begin{bmatrix} \ddot{\bar{\boldsymbol{X}}}_{d,B} \\ \ddot{\bar{\boldsymbol{X}}}_{d,\Gamma} \end{bmatrix} + \begin{bmatrix} \bar{\boldsymbol{K}}_{d,BB} & \bar{\boldsymbol{K}}_{d,B\Gamma} \\ \bar{\boldsymbol{K}}_{d,\Gamma B} & \bar{\boldsymbol{K}}_{d,\Gamma\Gamma} \end{bmatrix} \begin{bmatrix} \bar{\boldsymbol{X}}_{d,B} \\ \bar{\boldsymbol{X}}_{d,\Gamma} \end{bmatrix} = \begin{bmatrix} \boldsymbol{0} \\ \bar{\boldsymbol{F}}_{d,\Gamma} \end{bmatrix}; \tag{12}$$

where subscript d denotes the disk component; $\bar{\boldsymbol{F}}_d$ denotes the interface force matrix of disk component; $\bar{\boldsymbol{X}}_d$ and $\ddot{\bar{\boldsymbol{X}}}_{d,\Gamma}$ denote the interface displacement vector and the acceleration vector of disk component after transformation, respectively; $\bar{\boldsymbol{M}}_d$ and $\bar{\boldsymbol{K}}_d$ were the stiffness matrix and the mass matrix of disk component respectively, and can be expressed as:

$$\bar{\boldsymbol{M}}_d = \begin{bmatrix} \bar{\boldsymbol{M}}_{d,BB} & \bar{\boldsymbol{M}}_{d,B\Gamma} \\ \bar{\boldsymbol{M}}_{d,\Gamma B} & \bar{\boldsymbol{M}}_{d,\Gamma\Gamma} \end{bmatrix}, \quad \bar{\boldsymbol{K}}_d = \begin{bmatrix} \bar{\boldsymbol{K}}_{d,BB} & \bar{\boldsymbol{K}}_{d,B\Gamma} \\ \bar{\boldsymbol{K}}_{d,\Gamma B} & \bar{\boldsymbol{K}}_{d,\Gamma\Gamma} \end{bmatrix}. \tag{13}$$

The transformation relationship of the disk component before and after reduction can also be expressed as:

$$\bar{\boldsymbol{X}}_d = \begin{bmatrix} \boldsymbol{\varphi}_n & \boldsymbol{\psi}_m \end{bmatrix} \bar{\bar{\boldsymbol{X}}}_d = \begin{bmatrix} \bar{\boldsymbol{X}}_{d,B} & \bar{\boldsymbol{X}}_{d,\Gamma} \end{bmatrix}^T; \tag{14}$$

where $\ddot{\bar{\boldsymbol{X}}}_{d,B}$ denotes the reduced displacement vector of disk component; $\boldsymbol{\varphi_n}$ denotes the reduced displacement vector of disk component; $\boldsymbol{\psi}_m$ denotes the remaining set of m higher-order truncated modes of disk component.

By neglecting the influence of inertial forces, the Eq. (12) can be simplified to the static equation. And then, the coordinate transformation relationship Eq. (14) was substituted into it, the equation can be obtained as:

$$\bar{\boldsymbol{X}}_d = \boldsymbol{\varphi}_n \boldsymbol{K}_{nn}^{-1} \boldsymbol{\varphi}_n^{\mathrm{T}} \begin{bmatrix} \boldsymbol{0} \\ \bar{\boldsymbol{F}}_{d,\Gamma} \end{bmatrix} + \boldsymbol{\psi}_m \boldsymbol{K}_{mm}^{-1} \boldsymbol{\psi}_m^{\mathrm{T}} \begin{bmatrix} \boldsymbol{0} \\ \bar{\boldsymbol{F}}_{d,\Gamma} \end{bmatrix}; \tag{15}$$

in which

$$\boldsymbol{K}_{nn} = \boldsymbol{\varphi}_n^{\mathrm{T}} \bar{\boldsymbol{K}}_d \boldsymbol{\varphi}_n, \quad \boldsymbol{K}_{mm} = \boldsymbol{\psi}_m^{\mathrm{T}} \bar{\boldsymbol{K}}_d \boldsymbol{\psi}_m. \tag{16}$$

In addition, the residual flexibility matrix $\hat{\boldsymbol{G}}$, which reflects the flexibility contribution of the truncated higher-order modes of disk component, can be derived from Eq. (17):

$$\hat{\boldsymbol{G}} = \boldsymbol{G} - \bar{\boldsymbol{G}} = (\bar{\boldsymbol{K}}_d)^{-1} - \boldsymbol{\varphi}_k \boldsymbol{K}_{nn}^{-1} \boldsymbol{\varphi}_k^{\mathrm{T}} = \boldsymbol{\psi}_m \boldsymbol{K}_{mm}^{-1} \boldsymbol{\psi}_m^{\mathrm{T}}. \tag{17}$$

Next, using the solution method proposed by Li,[31] the modal matrix (i.e., the secondary reduced matrix) of disk component $\bar{\bar{\boldsymbol{U}}}_d$ can be derived as:

$$\bar{\bar{\boldsymbol{U}}}_d = \begin{bmatrix} \boldsymbol{I} & \boldsymbol{0} \\ \hat{\boldsymbol{G}}_{D\Gamma} \hat{\boldsymbol{G}}_{\Gamma\Gamma}^{-1} & \boldsymbol{\varphi}_{Dn} - \boldsymbol{\varphi}_{\Gamma n} \end{bmatrix}; \tag{18}$$

where subscript D denotes the internal DOFs of disk component.

Finally, the mass matrix $\bar{\bar{\boldsymbol{M}}}_d$ and the stiffness matrix $\bar{\bar{\boldsymbol{K}}}_d$ of disk component after secondary reduction were obtained and expressed as follows:

$$\bar{\bar{\boldsymbol{M}}}_d = (\bar{\bar{\boldsymbol{U}}}_d)^{\mathrm{T}} \bar{\boldsymbol{M}}_d \bar{\bar{\boldsymbol{U}}}_d, \quad \bar{\bar{\boldsymbol{K}}}_d = (\bar{\bar{\boldsymbol{U}}}_d)^{\mathrm{T}} \bar{\boldsymbol{K}}_d \bar{\bar{\boldsymbol{U}}}_d. \tag{19}$$

2.3. Modal Synthesis for Model Establishment

By assembling the HC blade and the disk components, the reduced free vibration equation of HC blisks was obtained as follows:

$$\begin{bmatrix} \bar{\bar{\boldsymbol{M}}}_b & \boldsymbol{0} \\ \boldsymbol{0} & \bar{\bar{\boldsymbol{M}}}_d \end{bmatrix} \begin{bmatrix} \ddot{\bar{\bar{\boldsymbol{X}}}}_b \\ \ddot{\bar{\bar{\boldsymbol{X}}}}_d \end{bmatrix} + \begin{bmatrix} \bar{\bar{\boldsymbol{K}}}_b & \boldsymbol{0} \\ \boldsymbol{0} & \bar{\bar{\boldsymbol{K}}}_d \end{bmatrix} \begin{bmatrix} \bar{\bar{\boldsymbol{X}}}_b \\ \bar{\bar{\boldsymbol{X}}}_d \end{bmatrix} = \boldsymbol{0}; \tag{20}$$

in which

$$\begin{bmatrix} \bar{\bar{\boldsymbol{X}}}_b \\ \bar{\bar{\boldsymbol{X}}}_d \end{bmatrix} = \begin{bmatrix} \bar{\bar{\boldsymbol{X}}}_{b,\Gamma} & \bar{\bar{\boldsymbol{X}}}_{b,B} & \bar{\bar{\boldsymbol{X}}}_{d,\Gamma} & \bar{\bar{\boldsymbol{X}}}_{d,B} \end{bmatrix}^{\mathrm{T}}; \tag{21}$$

and the coordinates used in Eq. (20) were then converted into the independent coordinates, according to the interface displacement compatibility condition between the HC blades and disk components, expressed in Eq. (22):

$$\boldsymbol{X}_{b,\Gamma} = \boldsymbol{X}_{d,\Gamma}. \tag{22}$$

The coordinates transformation formula for Eq. (20) was given in Eq. (23).

$$\begin{bmatrix} \bar{\bar{\boldsymbol{X}}}_{b,\Gamma} \\ \bar{\bar{\boldsymbol{X}}}_{b,B} \\ \bar{\bar{\boldsymbol{X}}}_{d,\Gamma} \\ \bar{\bar{\boldsymbol{X}}}_{d,D} \end{bmatrix} = \begin{bmatrix} \boldsymbol{I} & \boldsymbol{0} & \boldsymbol{0} \\ \boldsymbol{0} & \boldsymbol{I} & \boldsymbol{0} \\ \boldsymbol{I} & \boldsymbol{0} & \boldsymbol{0} \\ \boldsymbol{0} & \boldsymbol{0} & \boldsymbol{I} \end{bmatrix} \begin{bmatrix} \tilde{\boldsymbol{X}}_\Gamma \\ \tilde{\boldsymbol{X}}_{b,B} \\ \tilde{\boldsymbol{X}}_{d,D} \end{bmatrix} = \boldsymbol{\beta} \begin{bmatrix} \tilde{\boldsymbol{X}}_\Gamma \\ \tilde{\boldsymbol{X}}_{b,B} \\ \tilde{\boldsymbol{X}}_{d,D} \end{bmatrix}; \tag{23}$$

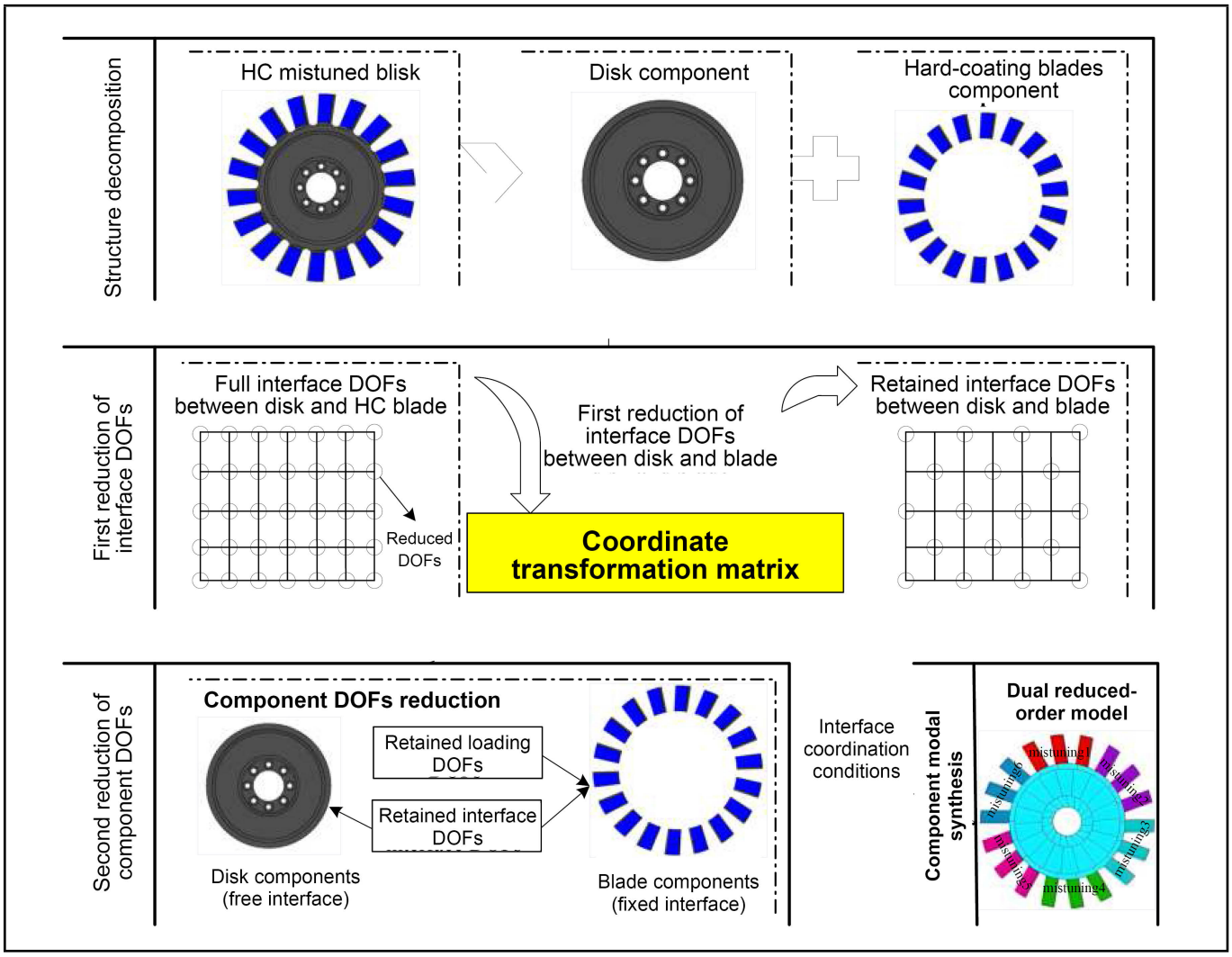

Figure 3. The second reduction of the component DOFs and modal synthesis of HC mistuned blisks.

where $\tilde{\boldsymbol{X}}_{\mathrm{b,B}}$ and $\tilde{\boldsymbol{X}}_{\mathrm{d,D}}$ were the internal displacement vectors of the reduced HC blade and the disk components, respectively; $\tilde{\boldsymbol{X}}_{\Gamma}$ denotes the interface displacement vector of the reduced component.

By combining Eq. (21) and Eq. (23), we can obtain the following result:

$$\begin{bmatrix} \bar{\bar{\boldsymbol{X}}}_b \\ \bar{\bar{\boldsymbol{X}}}_d \end{bmatrix} = \boldsymbol{\beta} \begin{bmatrix} \tilde{\boldsymbol{X}}_{\Gamma} & \tilde{\boldsymbol{X}}_{b,B} & \tilde{\boldsymbol{X}}_{d,D} \end{bmatrix}^{\mathrm{T}}. \tag{24}$$

By substituting Eq. (24) into Eq. (20) and premultiplying the resulting equation by $\boldsymbol{\beta}^T$, the integrated mass matrix $\tilde{\boldsymbol{M}}$ and stiffness matrix $\tilde{\boldsymbol{K}}$ of HC blisks were obtained as:

$$\tilde{\boldsymbol{M}} = \boldsymbol{\beta}^{\mathrm{T}} \begin{bmatrix} \bar{\bar{\boldsymbol{M}}}_b & \boldsymbol{0} \\ \boldsymbol{0} & \bar{\bar{\boldsymbol{M}}}_d \end{bmatrix} \boldsymbol{\beta}, \quad \tilde{\boldsymbol{K}} = \boldsymbol{\beta}^{\mathrm{T}} \begin{bmatrix} \bar{\bar{\boldsymbol{K}}}_b & \boldsymbol{0} \\ \boldsymbol{0} & \bar{\bar{\boldsymbol{K}}}_d \end{bmatrix} \boldsymbol{\beta}. \tag{25}$$

The Eq. (25) can be expanded further and expressed as:

$$\tilde{\boldsymbol{M}} = \boldsymbol{\beta}^{\mathrm{T}} (\bar{\boldsymbol{U}}\bar{\bar{\boldsymbol{U}}})^{\mathrm{T}} \begin{bmatrix} \boldsymbol{M}_b & \boldsymbol{0} \\ \boldsymbol{0} & \boldsymbol{M}_d \end{bmatrix} \bar{\boldsymbol{U}}\bar{\bar{\boldsymbol{U}}}\boldsymbol{\beta}; \tag{26a}$$

$$\tilde{\boldsymbol{K}} = \boldsymbol{\beta}^{\mathrm{T}} (\bar{\boldsymbol{U}}\bar{\bar{\boldsymbol{U}}})^{\mathrm{T}} \begin{bmatrix} \boldsymbol{K}_b & \boldsymbol{0} \\ \boldsymbol{0} & \boldsymbol{K}_d \end{bmatrix} \bar{\boldsymbol{U}}\bar{\bar{\boldsymbol{U}}}\boldsymbol{\beta}; \tag{26b}$$

$$\bar{\boldsymbol{U}} = \begin{bmatrix} \bar{\boldsymbol{U}}_b & \boldsymbol{0} \\ \boldsymbol{0} & \bar{\boldsymbol{U}}_d \end{bmatrix}, \quad \bar{\bar{\boldsymbol{U}}} = \begin{bmatrix} \bar{\bar{\boldsymbol{U}}}_b & \boldsymbol{0} \\ \boldsymbol{0} & \bar{\bar{\boldsymbol{U}}}_d \end{bmatrix}. \tag{27}$$

2.4. Vibration Analysis of the HC Mistuned Blisks

The kth angular frequency and corresponding mode shapes $\tilde{\boldsymbol{\varphi}}$ of HC mistuned blisks can be obtained from the characteristic's equation, which was shown as:

$$[\tilde{\boldsymbol{K}} - \omega_k^2 \tilde{\boldsymbol{M}}]\tilde{\boldsymbol{\varphi}} = \boldsymbol{0}; \tag{28}$$

and then, the natural frequency f_k of HC mistuned blisks can be solved as:

$$f_k = \frac{\omega_k}{2\pi}. \tag{29}$$

The hard coating deposited on the blades was treated as the proportional damping model, therefore the modal loss factors η_k of HC mistuned blisks can be obtained by the modal strain energy method:[32]

$$\eta_k = \bar{\eta}_c \frac{Y_{\mathrm{coating},k}}{Y_{\mathrm{blisk},k}}; \tag{30}$$

where $\bar{\eta}_c$ denote the material loss factor of hard coating; $Y_{\mathrm{coating},k}$ and $Y_{\mathrm{blisk},k}$ denote the kth mode strain energy of the hard coating and the mistuned blisks (substrate structure), respectively.

Then, the Rayleigh damping was used to substitute into the calculation model. The damping matrix $\tilde{\boldsymbol{D}}$ can be given by

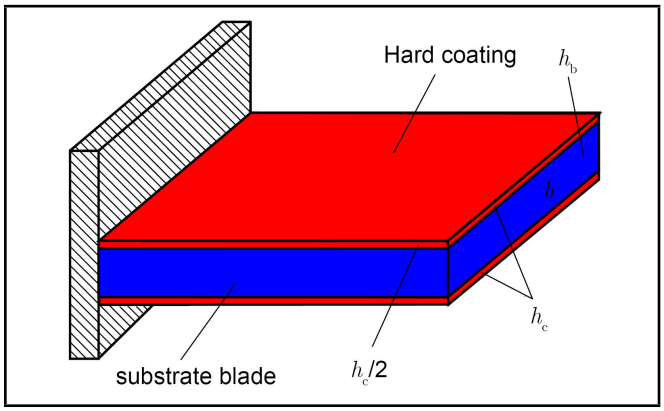

Figure 4. Schematic diagram of the blade deposited hard coating.

proportional constants g and l, combining with the mass matrix and the stiffness matrix, expressed as:

$$\tilde{\boldsymbol{D}} = q\tilde{\boldsymbol{M}} + l\tilde{\boldsymbol{K}}; \tag{31a}$$

$$g + l\omega_k^2 = \eta_k\omega_k. \tag{31b}$$

Finally, the forced vibration response $\tilde{\boldsymbol{X}}$ of HC mistuned blisks were solved under excitation force $\tilde{\boldsymbol{F}}$:

$$\left(\tilde{\boldsymbol{K}} + i\omega\tilde{\boldsymbol{D}} - \omega^2\tilde{\boldsymbol{M}}\right)\tilde{\boldsymbol{X}} = \tilde{\boldsymbol{F}}. \tag{32}$$

3. STRATEGIES FOR THE VIBRATION REDUCTION STRATEGY

3.1. Passive Vibration Reduction Strategy by The Damping Capacity of Hard Coating

For passive vibration reduction strategy of the mistuned blisks, the material damping capacity of hard coating was taken into consideration firstly. The schematic diagram of one typical HC blades was shown in Fig. 4. The hard coatings with uniform coating thickness of h_c were deposited on both sides of all blade substrate (its thickness was h_b). For the purpose of ensuring the satisfactory bonding state between the interface of the blade substrate and the hard coating layer, the hard coating layer in FEM was constructed by offsetting the blade surface with uniform thickness (the initial coating thickness was 0.2 mm, about 1% of blade thickness).

The HC blades, as the composite structures, can be equivalent to the homogeneous structure. In this process, the E_b and E_c were defined as the elastic modulus of the blade substrate and the hard coating layer, respectively; $\bar{\eta}_b$ and $\bar{\eta}_c$ were the material loss factors of that, respectively. By the derivation method developed in our previous research,[32] the equivalent elastic modulus E_{cb} and loss factor $\bar{\eta}_{\mathrm{cb}}$ of HC blade were obtained as:

$$E_{\mathrm{cb}} = \frac{1 + 2E_r(2h_r + 3h_r^2 + 2h_r^3) + E_r^2h_r^4}{(1 + E_rh_r)(1 + h_r)^3}E_b; \tag{33}$$

$$\bar{\eta}_{cb} = \bar{\eta}_b + \frac{E_rh_r}{(1 + E_rh_r)} \cdot \frac{(3 + 6h_r + 4h_r^2 + 2E_rh_r^3 + E_r^2h_r^4)}{(1 + 4E_rh_r + 6E_rh_r^2 + 4E_rh_r^3 + E_r^2h_r^4)}(\bar{\eta}_c - \bar{\eta}_b). \tag{34}$$

$$h_r = \frac{h_c}{h_b}, \quad E_r = \frac{E_c}{E_b}. \tag{35}$$

Considering that the elastic modulus and the loss factor of the blade will change simultaneously after the surface coating treatment, thus the complex modulus $\tilde{E}_{\mathrm{cb}}$ of HC blade, which enables the coupling of the stiffness and damping characteristics, can be further obtained as follows:

$$\tilde{E}_{\mathrm{cb}} = E_{\mathrm{cb}}\left(1 + i\bar{\eta}_{\mathrm{cb}}\right). \tag{36}$$

It was roughly predicted from Eqs. (33)–(36) that the elastic modulus and loss factor of mistuned blisks will also change after the surface coating treatment, which presents the forced vibration response of mistuned blisks that can be suppressed with natural frequency variation simultaneously. The specific influence of material damping capacity of hard coating on the vibration characteristics of the mistuned blisks will be addressed in detail in Section 4.3.

3.2. Hybrid Vibration Reduction Strategy by the Intentional Mistuning of Hard Coating

The elastic modulus and the loss factor of mistuned blisks vary consistently with coating thickness variations, this thereby provides a novel strategy for the hybrid vibration reduction of mistuned blisks, which can be realized by intentional mistuning (it was small mistuning) designed by the various coating thickness. Here, the intentional stiffness and damping mistuning variations of the pth HC blade were realized by means of the variations of the elastic modulus $\Delta E_{\mathrm{c},p}$ and the loss factor $\Delta\bar{\eta}_{\mathrm{c},p}$ of hard coating, which can be obtained as:

$$\Delta E_{\mathrm{c},p} = E_c\Delta q; \tag{37a}$$

$$\Delta\bar{\eta}_{\mathrm{c},p} = \bar{\eta}_c\Delta q; \tag{37b}$$

where Δq denotes the expression form of intentional mistuning patterns. The Harmonic-wave mistuning pattern was considered in this paper, and the Δq can be expressed in detail as:

$$\Delta q = AH, H = \sin\left(\frac{2\pi Qp}{P}\right); \tag{38}$$

where A denotes the maximum value of intentional mistuning, p denotes the number order of HC blade, P denotes the total number of all HC blades, Q denotes the wave number and determined as 2 here. The results of H in Eq. (38) which reflect the variation rule of intentional mistuning were solved in Fig. 5.

Finally, by combining Eqs. (37a) and (37b) with (38), the elastic modulus $E_{\mathrm{c},p}$ and the loss factor $\bar{\eta}_{\mathrm{c},p}$ of hard-coating blades with the intentional Harmonic-wave mistuning can be expressed as:

$$E_{\mathrm{c},p} = E_c\left[1 + A_E\sin\left(\frac{2\pi Q_wp}{P}\right)\right]; \tag{39}$$

$$\bar{\eta}_{\mathrm{c},p} = \bar{\eta}_c\left[1 + A_L\sin\left(\frac{2\pi Q_wp}{P}\right)\right]; \tag{40}$$

where A_E and A_L denote the maximum value corresponding to the elastic modulus and loss factor.

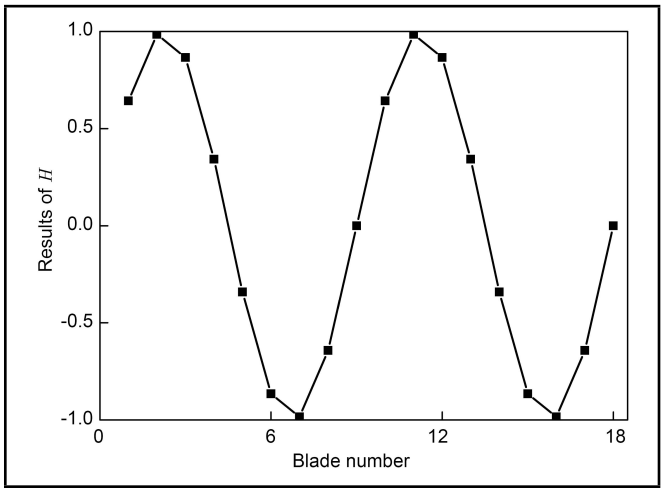

Figure 5. Intentional mistuning quantities of each HC blade.

As reported in the literature, the optimal vibration suppression of mistuned blisks can be achieved with small intentional mistuning, which effectively reduces the forced response while causing only minimal natural frequency variations.[32] So, the magnitude of intentional damping mistuning should exceed that of intentional stiffness mistuning. Here, the maximum variation of intentional mistuning generated by the various coating thickness was set as 10%. By the Eq. (33) and Eq. (34), the maximum value of the elastic modulus A_E and the loss factor A_L were determined as 1.6% and 3.1, respectively. The specific influence of intentional mistuning designed by hard coating on hybrid vibration reduction of the mistuned blisks will be investigated comprehensively in Section 4.4.

4. BENCHMARK CASE

4.1. Description of the HC Mistuned Blisks and Test Condition

A mistuned blisks specimen manufactured by the wire-electrode cutting technique was taken as the benchmark case in this paper. The mistuned blisks specimen with 18 sectors and the blades deposited NiCrAlY hard coating (the blade surface treatment was conducted by the atmospheric plasma spraying technology) were shown in Fig. 6.

The mistuned blisk specimen was rigidly connected to a dedicated fixture using eight high-strength bolts with a tightening torque of 40 Nm. Moreover, the inherent mistuning levels of each blade were obtained by normalizing the natural frequencies of mistuned blisk specimen, as illustrated in Fig. 7. And these natural frequencies of mistuned blisks were obtained by the hammer-peening method, as illustrated in Fig. 8. In which, some professional testing devices, including but not limited to the PCB® modal hammer, the BK®-4517 accelerometer, LMS® mobile front-end controller and DELL® mobile workstation, were used together to solve the natural characteristics of mistuned blisks specimen before and after surface coating treatment.

In addition, the geometric parameters and the mechanical parameters associated with the mistuned blisks specimen and the NiCrAlY hard coating were listed in Table 1 and Table 2, respectively. It should be noted that the elastic modulus and the loss factor of NiCrAlY hard coating was obtained by the identifiable investigation at room temperature, whose discrete data was equivalently processed and verified here.

(a) mistuned blisk

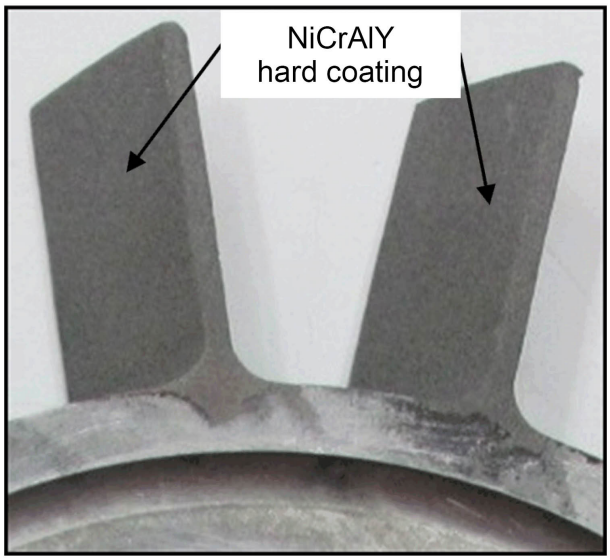

(b) hard-coating blades

Figure 6. The solid model of mistuned blisks and the blades deposited hard coating.

4.2. Vibration Analyses for Model Validation

The corresponding full stage FEM of HC mistuned blisks, as shown in Fig. 9(a), was established using the 3D SOLID185 elements, whose numbers of the elements and the DOFs were 385992 and 1.337 million, respectively. And then, the ROM of the HC mistuned blisks was built by using the improved component method developed in Section 2. The DOFs numbers of the established ROM was about 203224, which were reduced by 85% approximately compared with that of full stage FEM.

In the calculation process, the loading location of excitation force along the axial direction, and the pick-up location of vibration response of HC blisks were the tip nodes of HC blades. And the natural frequencies and mode shapes of HC mistuned

Table 1. Geometrical parameters of the mistuned blisks and the hard coating.

Component catalog	Geometric parameters	Value	Component catalog	Geometric parameters	Value
blades	length	50 mm	disk	inner radius	50 mm
	width	25 mm		outer radius	200 mm
	thickness	3 mm		thickness	20 mm
	number	18	hard coating	area ratio	100%
	installation angle	45°		thickness	0.2 0mm

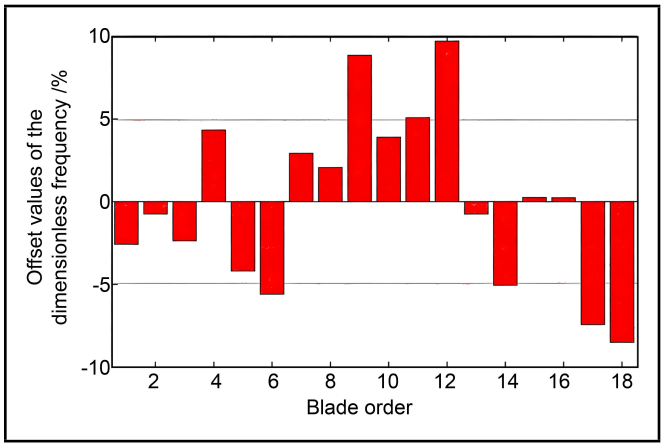

Figure 7. Dimensionless natural frequency deviation values of blades.

Table 2. Material parameters of the mistuned blisks and the hard coating.

Component catalog	blades	disk	hard coating
Material type	Q235 steel	Q235 steel	NiCrAlY
Elastic modulus (GPa)	208	208	54.5
Mass density (kg/m^3)	7860	7860	2840.7
Material loss factor	0.0005	0.0005	0.0099
Poisson's ratio	0.277	0.277	0.300

blisks can be solved using the established ROM. Moreover, a testing model of HC mistuned blisks was established in the LMS Test Lab, as shown in Fig. 9(b). The excitation points in the hammer-peening test were consistent with the axial blade tip excitation position used in the above finite element simulation. Then, the natural frequencies and mode shapes of HC mistuned blisks can be obtained by the testing model.

The first fifteen orders natural frequencies of HC mistuned blisks obtained from the ROM and the test model were listed in Table 3. For the explicit verification of data accuracy, its relative errors (absolute value) were also solved and listed. It clearly shows that relative errors of natural frequencies obtained by the two methods exist, with the relative errors ranging from 0.36% to 5.86%. The larger errors for the 11th and 12th modes were caused by the modal truncation in the established ROM. However, these high-order modes were not within the main resonance region of the mistuned blisk, such errors did not affect the accuracy of vibration response suppression in the studied frequency band. Moreover, the average relative error was 3.35%, and the maximum relative error was limited to 6%. Overall, the natural frequencies of hard-coated mistuned blisks calculated by the established ROM can be considered acceptable here.

The first eight orders mode shapes of HC mistuned blisks obtained from the established ROM were presented in Appendix section. For the explicit verification of data accuracy, the modal assurance criterion (MAC)[34,35] was employed widely to evaluate the correlation of mode shapes originating from different models, always range from 0.0 to 1.0, and the higher MAC value indicates the higher similarity between mode shapes. Commonly, if the value was lower than 0.8, the mode shape correlation was generally considered poor, and the simulation model needs to be modified. The first fifteen MACs of HC mistuned blisks between the ROM and the test model were calculated and shown in Fig. 10. It can be seen that the MAC values for the same mode order (marked in blue at the upper-right diagonal position) were all larger than 0.875, nearly to 1.0, and the other MAC values were close to 0. In general, mode shapes of HC mistuned blisks obtained by the ROM were accurate and can be accepted here.

Table 3. Natural frequencies and percent errors of the HC mistuned blisks obtained by the ROM and the test.

Mode order	ROM / Hz	Test / Hz	Relative error / %
1	663.07	660.71	0.36
2	667.36	670.48	0.47
3	677.60	686.04	1.25
4	684.78	696.52	1.71
5	689.26	709.49	2.94
6	699.17	721.11	3.14
7	702.78	731.14	4.04
8	712.21	744.03	4.47
10	729.46	765.55	4.95
11	731.79	774.64	5.86
12	746.29	786.62	5.4
13	757.02	797.35	5.33
14	1236.98	1260.92	1.94
15	1341.56	1389.98	3.61

The first fifteen order modal loss factors of HC mistuned blisks, an important parameter for evaluating damping capacity, obtained from two different ways were plotted in Fig. 11. In which, the blue solid lines with square symbols represent the modal loss factors obtained from the ROM, and the red dashed lines with circular symbols were the modal loss factors obtained from the test model. It can be observed that the small deviations among these results exhibit at the same mode order (the maximum deviation was less than 1%), and the results trends were nearly consistent. In general, the modal loss factors of HC mistuned blisks from the ROM were reliable here.

On the premise of ensuring calculation accuracy, the solution efficiency for vibration characteristics of the ROM was investigated. Under the same computational platform, the vibration analysis of HC blisks was also conducted using the full stage FEM. And the first 130 orders time-consuming ratios (defined as $\frac{t_{\mathrm{ROM}}}{t_{\mathrm{FEM}}}$) were calculated and expressed in Fig. 12. It can be found that compared with the full stage FEM, the computational efficiency of the ROM was enhanced by at least 85%. In addition, the higher the mode was, the more efficient the ROM will be.

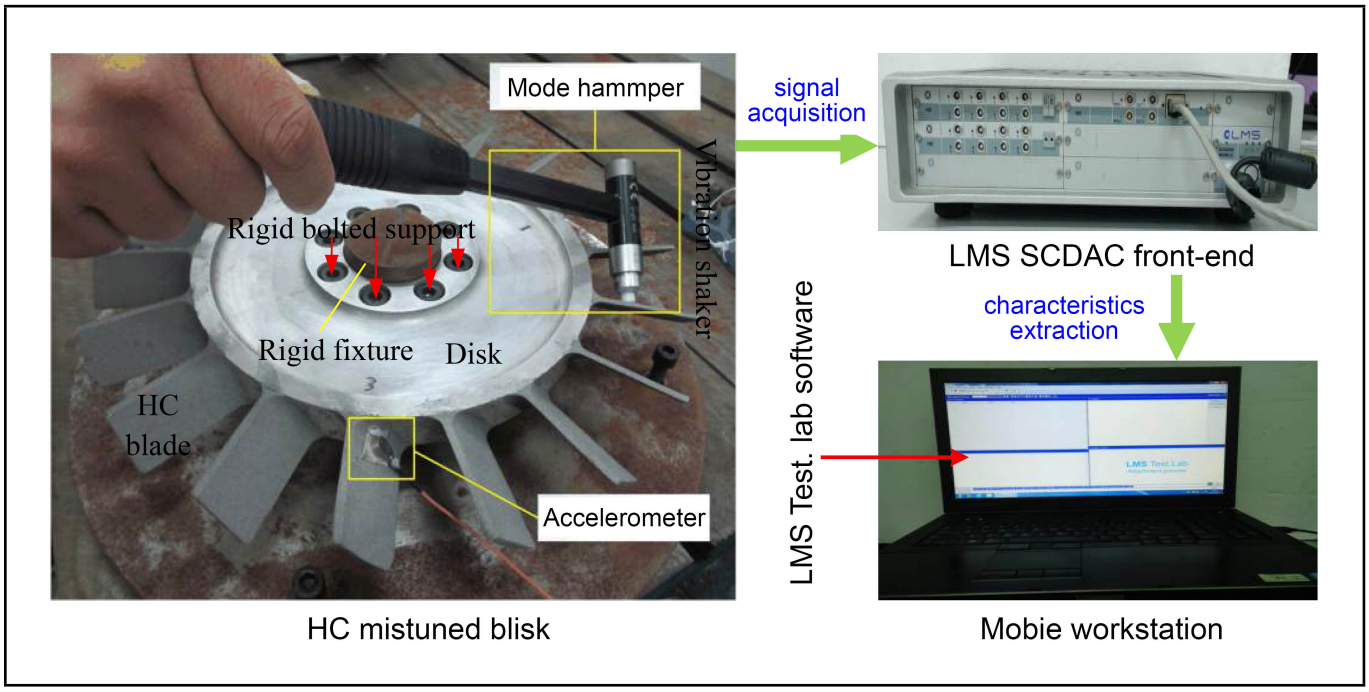

Figure 8. Testing condition for of the HC mistuned blisks.

4.3. Damping Vibration Reduction Analysis

Using the reliable ROM established in Section 2, the damping vibration reduction analysis for mistuned blisk was conducted here. The coating thickness of different blades were uniform (about 0.2 mm), the specific influence of material damping capacity of hard coating on the mistuned blisks were detailly discussed in terms of natural frequencies and forced responses, which can provide a reference for the selection of intentional mistuning parameters.

Natural frequencies of the mistuned blisks and the HC mistuned blisks were listed in Table 4, and its change rates were also solved for the quantitative evaluation. It can be found exactly that natural frequencies of mistuned blisks were lower than that of HC mistuned blisks generally, but all the change rates were limited to 2%. Moreover, these corresponding results obtained from the test model were also obtained for numerical validation, whose change rates always range from 0.45% to 3.49%. Generally, the influence of NiCrAlY hard coating on natural frequencies of mistuned blisks was relatively weak.

The forced responses of each blade (remarked by the left red bars and defined as "no coating") and HC blade (remarked by the right blue bars and defined as "uniform coating") obtained from the ROM under same exaction were shown in Fig. 13(a), and its responses decreased rates were also solved for elaborating quantitatively on the damping vibration reduction performance of hard coating, as plotted in Fig. 13(b). It can be seen clearly that the forced responses of all blades were suppressed obviously by the hard coating, and the response decreased rates were larger than 20% commonly.

Moreover, the maximum responses of the mistuned blisks (marked by solid lines) and the HC mistuned blisks (marked by dashed line) in frequency domain were shown in Fig. 14. From the perspective of horizontal coordinates, resonant frequency of mistuned blisks decrease slightly, which was consistent with the results variation trend showed in Table 4; meanwhile, the forced vibration response of mistuned blisks was less than that of HC mistuned blisks remarkable from the perspective of vertical coordinates, which was consistent with the results variation trend showed in Fig. 13. In general, the NiCrAlY hard coating has a significant performance on damping vibration reduction of mistuned blisks without altering natural frequencies significantly.

4.4. Hybrid Vibration Reduction Analysis

According to the foregoing research, the small intentional mistuning of each blade designed by various coating thickness was conducted for the hybrid vibration reduction of mistuned blisks, and the forced responses of HC mistuned blisks with dual mistuning (including the blades intrinsic mistuning and the intentional mistuning induced by hard coating), called DHC mistuned blisks, were solved effectively by using the reliable ROM.

The forced responses of each blade of DHC mistuned blisks (remarked as green bars and defined as "intentional coating") were shown in Fig. 15(a). And, the forced responses of each blade (remarked by the red bars and defined as "no coating") and HC blade (remarked by the blue bars and defined as "uniform coating") were also shown for comparison straightforwardly. It can be seen exactly that the forced responses of mistuned blisks were largest, and that of HC mistuned blisks were intermediate, and that of DHC mistuned blisks and mistuned blisks were the smallest. Moreover, the corresponding response decreased rates between DHC mistuned blisks and mistuned blisks (marked by blue lines and defined as "intentional coating/no coating" or "IN"), between DHC mistuned blisks and HC mistuned blisks (marked by red lines and defined as "intentional coating/uniform coating" or "IU") were obtained for quantitative analysis, as shown in Fig. 15(b). It can be found that the response decreased rates of "IN" were larger that of "IU", which indicates the vibration reduction performance of mistuned blisk was further enhanced obviously

Table 4. Natural frequencies of the mistuned and HC mistuned blisks obtained by the ROM and the test.

Mode order	ROM			Testing model		
	Mistuned blisks / Hz	HC mistuned blisks / Hz	Change rate / %	Mistuned blisks / Hz	HC mistuned blisks / Hz	Change rate / %
1	653.03	663.07	1.54	655.73	660.71	0.75
2	658.69	667.36	1.32	665.09	670.48	0.80
3	667.50	677.60	1.51	678.42	686.04	1.11
4	674.80	684.78	1.48	688.14	696.52	1.20
5	679.09	689.26	1.50	702.45	709.49	0.99
6	690.74	699.17	1.22	711.56	721.11	1.33
7	694.83	702.78	1.14	721.36	731.14	1.34
8	703.05	712.21	1.30	731.18	744.03	1.73
9	711.84	723.13	1.58	739.11	754.55	2.05
10	716.34	729.46	1.79	747.40	765.55	2.37
11	720.31	731.79	1.59	753.87	774.64	2.68
12	734.57	746.29	1.60	764.19	786.62	2.85
13	744.91	757.02	1.63	778.81	797.35	2.33
14	1215.94	1236.98	1.73	1221.97	1260.92	3.09
15	1317.40	1341.56	1.83	1341.48	1389.98	3.49

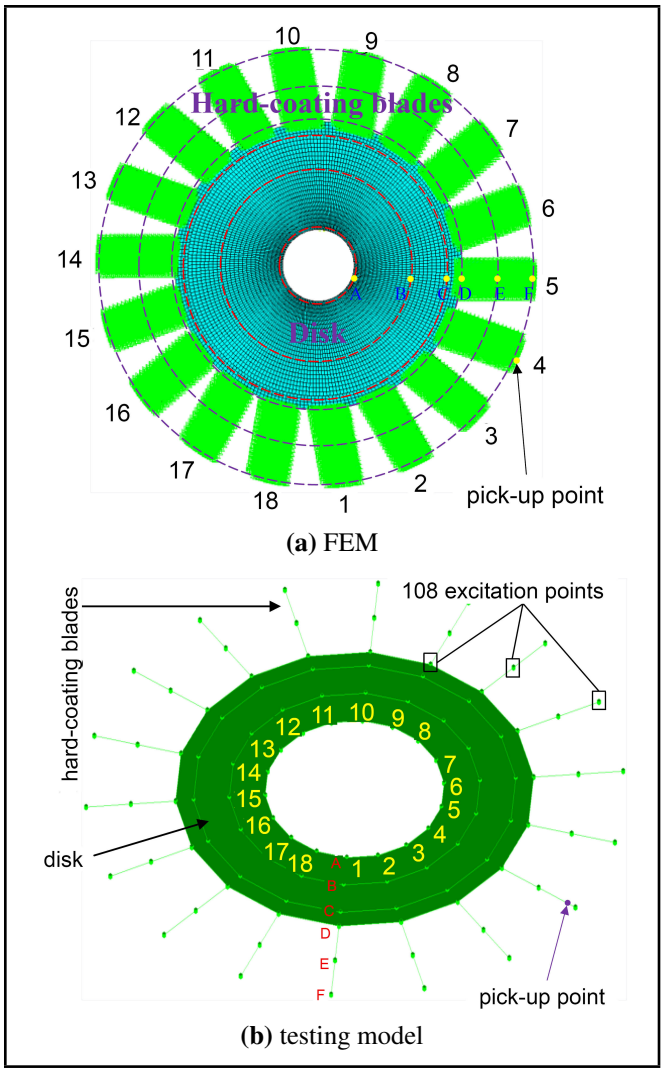

Figure 9. Vibration models of the HC mistuned blisks.

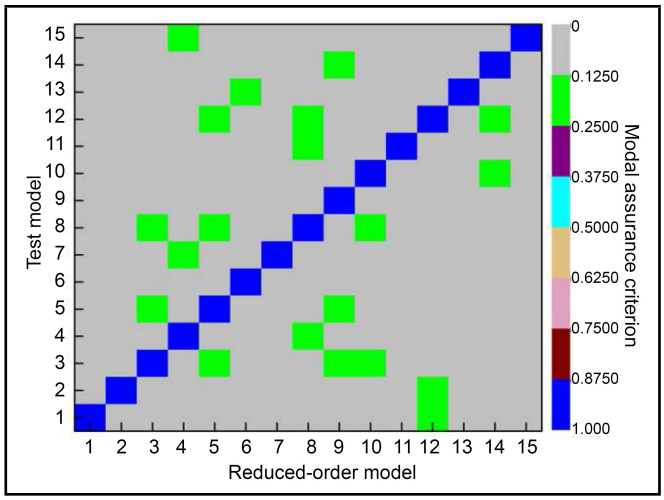

Figure 10. Modal assurance criterion of the HC mistuned blisks obtained between the ROM and the test.

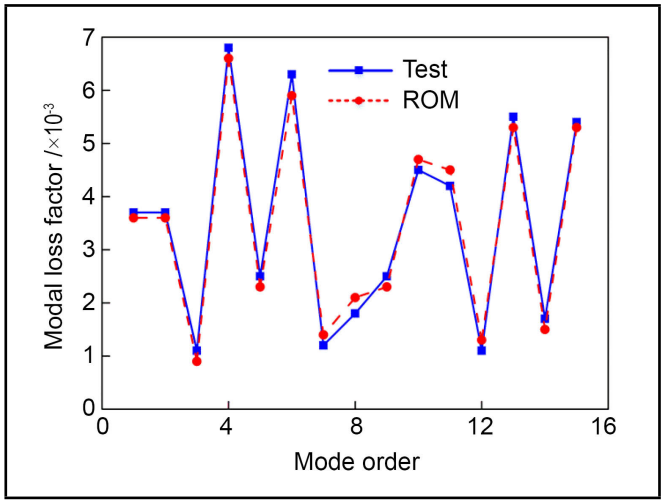

Figure 11. Modal loss factors of the HC mistuned blisks.

by the intentional mistuning. It can be attributed to the fact that the passive vibration reduction method merely utilizes the damping capacity of hard coating, whereas the hybrid vibration reduction method integrates two mechanisms, namely damping capacity and intentional mistuning.

In addition, the maximum frequency-domain responses of the DHC mistuned blisks under same exaction was shown in Fig. 16. Compared the results of line A, the forced responses of mistuned blisk, presented by line C, were suppressed remarkably; compared the results of line B, the forced responses of mistuned blisk were further suppressed obviously, which indicated that the hybrid vibration reduction strategy was superior to the passive damping reduction strategy. This charac-

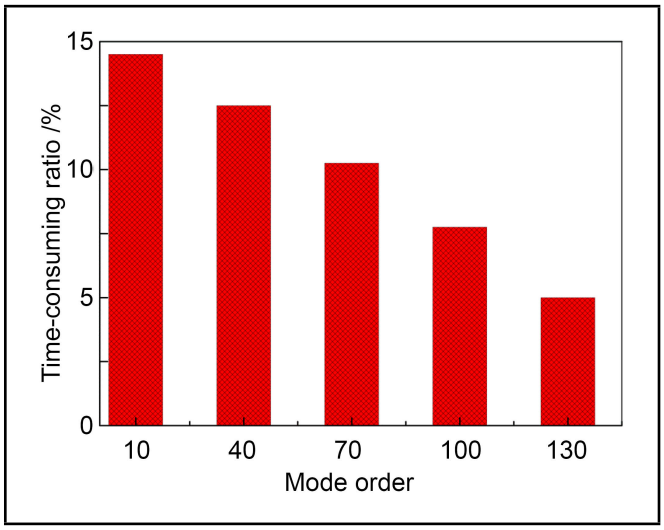

Figure 12. Ratios of computational time of the HC mistuned blisks.

teristic shows an excellent consistency with that illustrated in Fig. 15. From the perspective of horizontal coordinates, resonant frequency of mistuned blisks decreased slightly, which was consistent with the results variation trend showed in Table 4; meanwhile, the forced vibration response of mistuned blisks was less than that of HC mistuned blisks remarkable from the perspective of vertical coordinates, which was consistent with the results variation trend showed in Fig. 13.

5. CONCLUSION

For the vibration reduction of mistuned blisks effectively, a novel strategy by the intentional mistuning of hard coating damping was developed. Then, by the improved component method, a reliable ROM of HC mistuned blisks was established for solving vibration characteristics and verifying vibration reduction strategies efficiently.

By combining the first reduction of interface DOFs and the second reduction of components DOFs, an efficient ROMof mistuned was established for model validation. Compared with the test model and full stage FEM, the calculation precision and efficiency of the established ROM was verified. It laid a reliable foundation for the investigation on passive vibration reduction strategy by the damping capacity of hard coating.

The NiCrAlY hard coating was deposited on both sides of all blades with uniform coating thickness, and the passive damping vibration reduction strategy for mistuned blisks was conducted. The results reveal that the forced responses of mistuned blisk were suppressed remarkably by the hard coating with decreasing natural frequencies slightly. It was mainly attributed to the material damping capacity of the hard coating. This lays a reliable foundation for the hybrid vibration reduction strategy by the small intentional mistuning of hard coating damping.

The hybrid vibration reduction strategy by the intentional mistuning of hard coating was then conducted. The results reveal that the forced responses of mistuned blisks can be further suppressed obviously based on the damping vibration reduction, which indicated the hybrid vibration reduction strategy for mistuned using two mechanisms simultaneously was better than the passive vibration reduction strategy using single

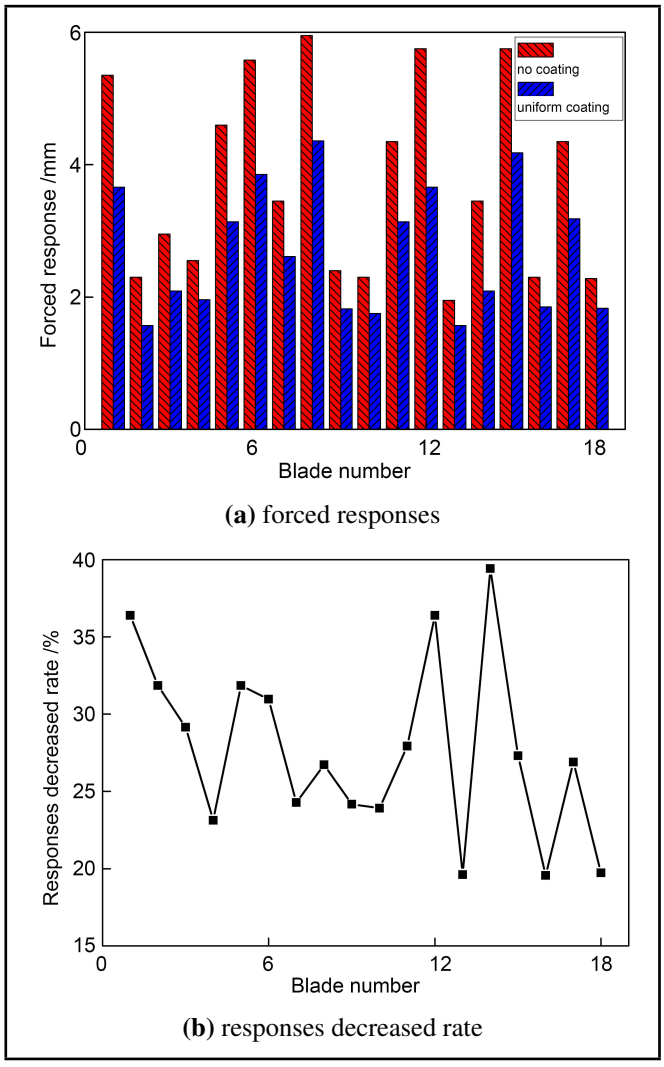

Figure 13. Forced responses of each blade and HC blade and its decreased rates.

mechanisms.

In addition, the hybrid vibration reduction strategy proposed in this study features more flexible and broader applicability. It can effectively suppress the vibration localization caused by different degrees of passive mistuning by applying a hard coating with different thicknesses and types at various positions.

ACKNOWLEDGEMENT

The authors were very grateful for financial support from the Wuxi "Taihu Light" Science and Technology Research (Basic Research Category) of China (Grant No. K20231019).

REFERENCES

[1] Aschenbruck, J., Adamczuk, R., and Seume, J. R. Recent progress in turbine blade and compressor blisks regeneration, *Procedia CIRP*, **22**, 256–262, (2014). https://doi.org/10.1016/j.procir.2014.07.016

[2] Li, A., Wang, W., Fan, Y., et al. Mistuning identification of blisks based on antiresonance, *Mechanical Systems and Signal Processing*, **239**, 113307, (2025). https://doi.org/10.1016/j.ymssp.2025.113307

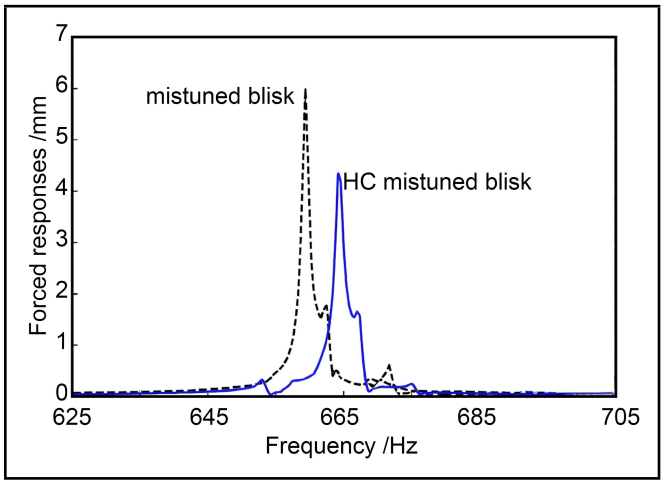

Figure 14. Maximum forced response of the mistuned blisks and the HC mistuned blisks.

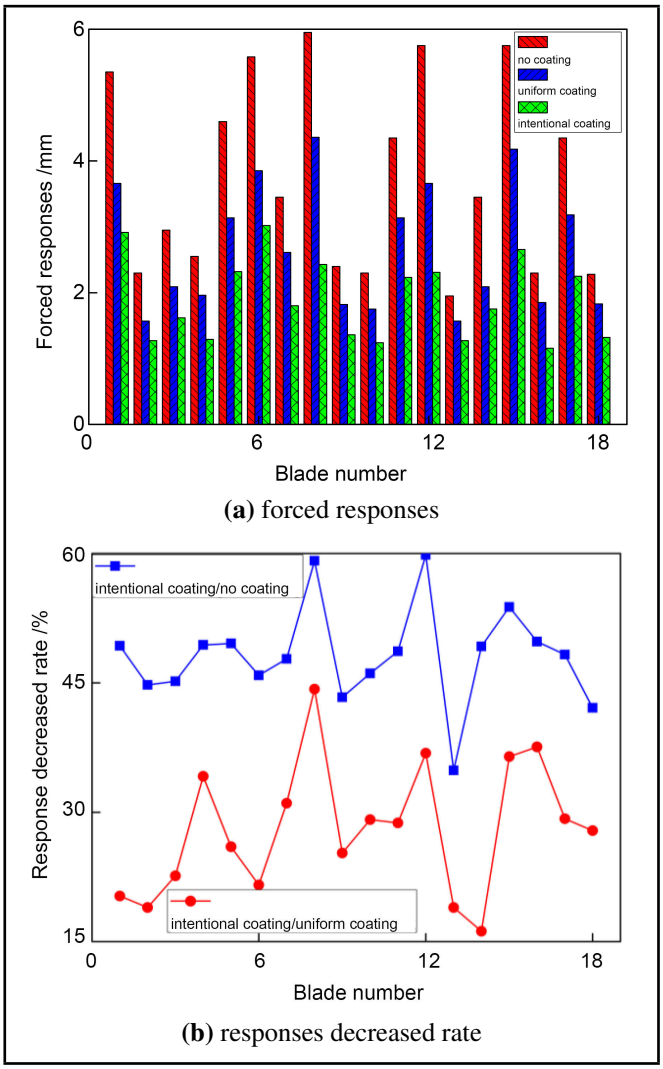

Figure 15. Forced responses of each blade, HC blade, DHC blade and its decreased rates.

[3] Xu, Q., Hou, L., Hou, L., et al. A novel ROM-based FSI model of composite blisks with blades-disk coupling for flutter analysis, *Aerospace Science and Technology*, **159**, 109961, (2025). https://doi.org/10.1016/j.ast.2025.109961

[4] Xie, W., Song, Y., Chen, Y., et al. Analysis of excitation force on aeroengine blisks structure, *Proc. of International Conference on Mechanical Design and Simulation*, 825–834, (2024).

[5] Krizak, T., Kurstak, E., and D'Souza, K. Experimental and computational study of a rotating bladed disk with under-platform dampers, *AIAA Journal*, **61**(10), 4717–4727, (2023). https://doi.org/10.2514/1.J062752

[6] Ferhatoglu, E., Gastaldi, C., Botto, D., et al. An experimental and computational comparison of the dynamic response variability in a turbine blade with under-platform dampers, *Mechanical Systems and Signal Processing*, **172**, 108987, (2022). https://doi.org/10.1016/j.ymssp.2022.108987

[7] Wu, Y. G., Wang, H., Fan, Y., et al. On the network of synchronized switch damping for blisks, *Mechanical Systems and Signal Processing*, **184**, 109695, (2023). https://doi.org/10.1016/j.ymssp.2022.109695

[8] Shen, J., Sun, W., Xu, K., et al. Vibration suppression of the blisks based on intentional mistuning of piezoelectric shunt damping patches, *Mechanics of Advanced Materials and Structures*, **31**(26), 7870–7886, (2024). https://doi.org/10.1080/15376494.2023.2251193

[9] Shen, J., Sun, W., Xu, K., et al. Optimization analysis of the intentional mistuning mode of the blisks with piezoelectric shunt damping patches, *Journal of the Brazilian Society of Mechanical Sciences and Engineering*, **46**(1), 3, (2024). https://doi.org/10.1007/s40430-023-04583-2

[10] Li, A., Fan, Y., Wang, H., et al. Mistuning identification and model updating of a blisks with piezoelectric excitation components, *Journal of Vibration and Control*, **30**(23-24), 5214–5227, (2024). https://doi.org/10.1177/10775463231218481

[11] Duan, Y. and Huo, L. Pounding tuned mass damper with constrained layer damping, *Advances in Structural Engineering*, **26**(11), 1301–1313, (2023). https://doi.org/10.1177/13694332221149484

[12] Couet, M., Jean-François Deü, Rouleau, L., et al. Impact of constrained layer damping patches on the dynamic behavior of a turbofan bladed disk, *Journal of Sound and Vibration*, **606**, 119002, (2025). https://doi.org/10.1016/j.jsv.2025.119002

[13] Wang, S., Wang, F., Chen, H., et al. The vibration attenuation characteristics of dynamic vibration absorbers array for tuned and mistuned bladed disk, *Journal of Engineering for Gas Turbines and Power*, **145**(10), 101008, (2023). https://doi.org/10.1115/1.4063228

[14] Wu, Y. G., Fan, Y., Li, L., et al. On the performance of wavy dry friction and piezoelectric hybrid flexible dampers, *Journal of Engineering for Gas Turbines and Power*, **143**(12), 121010, (2021). https://doi.org/10.1115/1.4051955

[15] Sun, Y., Yuan, J., Denimal, E., et al. Nonlinear modal analysis of frictional ring damper for compressor blisks, *Journal of Engineering for Gas Turbines and Power*, **143**(3), 031008, (2021). https://doi.org/10.1115/1.4049761

[16] Lupini, A. and Epureanu, B. I. A friction-enhanced tuned ring damper for bladed disks, *Journal of Engineering for Gas Turbines and Power*, **143**(1), 011002, (2021). https://doi.org/10.1115/1.4049203

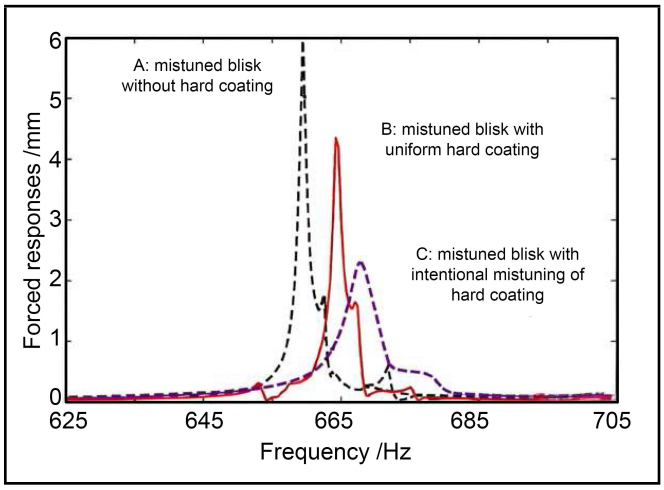

Figure 16. Forced response of the mistuned blisks with intentional mistuning of hard coating.

[17] Sun, W., Li, R., and Jiang, J. Lumped-parametric modeling based on modal test and analysis of vibration characteristics of the hard-coated blisks, *Journal of Vibration Engineering & Technologies*, **7**(4), 347–358, (2019). https://doi.org/10.1007/s42417-019-00127-y

[18] Bai, B., Xiang, L., Zeng, X., et al. Vibration characteristics investigation of hard-coated mistuned blisks with multi-packets by lumped parameter model, *Journal of Engineering for Gas Turbines and Power*, **146**(10), 101003, (2024). https://doi.org/10.1115/1.4065141

[19] Gao, F. and Sun, W. Free vibration analysis of the hard-coating splitter blisks using the energy-based finite element method, *Proceedings of the Institution of Mechanical Engineers, Part C: Journal of Mechanical Engineering Science*, **233**(13), 4577–4589, (2019).

[20] Gao, F., Sun, W., and Gao, J. Optimal design of the hard-coating blisks using nonlinear dynamic analysis and multi-objective genetic algorithm, *Composite Structures*, **208**, 357–366, (2019). https://doi.org/10.1016/j.compstruct.2018.10.031

[21] Gao, J., Gao, Y., Yan, X., et al. Damping mistuning effect of the hard-coating-based intentional mistuning techniques on mistuned blisks and its mechanism, *Aerospace Science and Technology*, **101**, 105848, (2020). https://doi.org/10.1016/j.ast.2020.105848

[22] Yan, X., Sun, W., Du, D., et al. Effects of nonlinear coatings on vibration characteristics of rotating blisks with mistuning features, *Engineering Failure Analysis*, **128**, 105632, (2021). https://doi.org/10.1016/j.engfailanal.2021.105632

[23] Xu, K., Yan, X., Xu, D., et al. Detection of blade substrate crack parameters of hard-coated blisks based on mistuning identification technology, *Mechanical Systems and Signal Processing*, **165**, 108381, (2022). https://doi.org/10.1016/j.ymssp.2021.108381

[24] Castanier, M. P., Ottarsson, G., and Pierre, C. A reduced order modeling technique for mistuned bladed disks, *Journal of Vibration and Acoustics*, **119**(3), 439–447, (1997). https://doi.org/10.1115/1.2889743

[25] Gutierrez Salas, M., Petrie-Repar, P., Mårtensson, H., et al. Forced response analysis of a mistuned blisks using noncyclic reduced-order models, *Journal of Propulsion and Power*, **34**(3), 565–577, (2018). https://doi.org/10.2514/1.B36584

[26] Gao, F., Li, B., and Liu, X. Passive vibration reduction analysis of the mistuned blisks deposited hard coating using modified reduced-order model, *Coatings*, **9**(12), 812, (2019). https://doi.org/10.3390/coatings9120812

[27] Gao, F., Sun, W., and Jiang, L. Application of the hard coating on the mistuned blisks for passive vibration reduction, *Proceedings of the Institution of Mechanical Engineers, Part C: Journal of Mechanical Engineering Science*, **233**(5), 1562–1574, (2019). https://doi.org/10.1177/0954406218771999

[28] Xu, K., Yan, X., Du, D., et al. Identification and influence factors analysis of blade crack mistuning in hard-coated blisks based on modified component mode mistuning reduced-order model, *Journal of Low Frequency Noise, Vibration and Active Control*, **40**(3), 1401–1424, (2021). https://doi.org/10.1177/1461348420971382

[29] Nie, W., Cao, Z. F., Jiang, D., et al. Vibration performance analyzing of stitched sandwich panel based on repetitive substructure, *Acta Materiae Compositae Sinica*, **37**(2), 482–491, (2020). https://doi.org/10.13801/j.cnki.fhclxb.20190701.003

[30] Li, X. Q., Dang, Z. X., Li, C. B., et al. Substructure normal modes selection method for component mode synthesis, *Journal of Southwest Jiaotong University*, **27**(1), 173–178, (2014). https://doi.org/10.3969/j.issn.0258-2724.2014.01.027

[31] Li, R. Y., Liu, J. W., and Yao, J. Y. Application of mode synthesis method for vibration analysis of geometrically mistuned bladed disk considering the prestress, *Chinese Journal of Turbomachinery*, **61**(5), 72–78, (2019).

[32] Gao, F., Sun, W., and Gao, J. Vibration characteristics study for the hard coating blisks using finite element method, *Journal of Northeastern University (Natural Science)*, **40**(5), 688–693, (2019).

[33] Chen, Y., Zhai, J., and Han, Q. Vibration and damping analysis of the bladed disk with damping hard coating on blades, *Aerospace Science and Technology*, 248–257, (2016). https://doi.org/10.1016/j.ast.2016.08.016

[34] Greś, S., Döhler, M., and Mevel, L. Uncertainty quantification of the modal assurance criterion in operational modal analysis, *Mechanical Systems and Signal Processing*, **152**, 107457, (2021). https://doi.org/10.1016/j.ymssp.2020.107457

[35] Hızal, Ç. A Bayesian approach to global mode shape identification using modal assurance criterion-based discrepancy model, *Journal of Sound and Vibration*, **558**, 117774, (2023). https://doi.org/10.1016/j.jsv.2023.117774

APPENDIX

The Appendix section illustrates the partial mode shapes of the HC blisks obtained by the simulations for full stage FEM and ROM (see Fig. 17), and the partial mode shapes of the HC blisks obtained by the experimental testing (see Fig. 18).

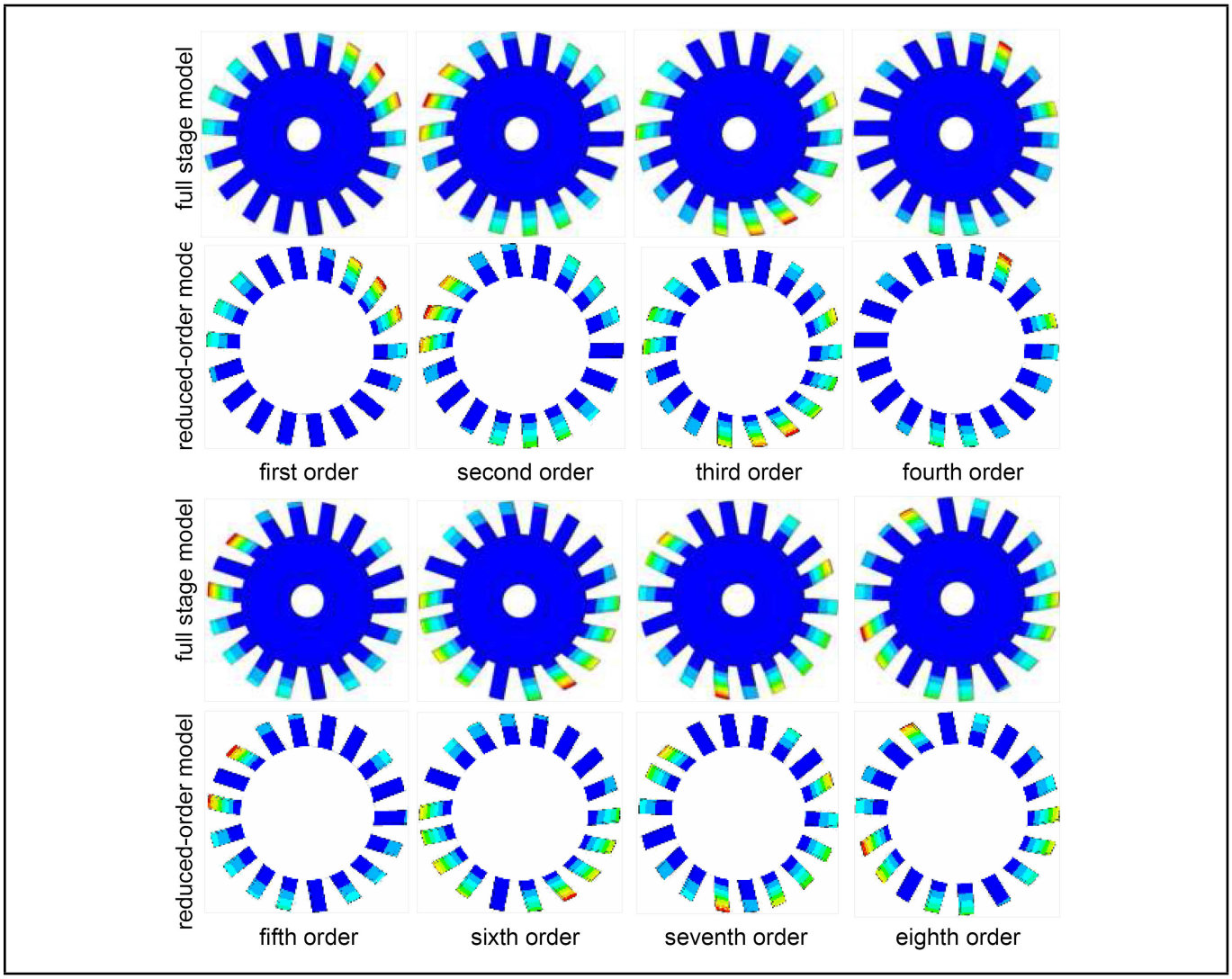

Figure 17. Partial mode shapes of the HC blisks obtained by the simulations (full stage FEM and ROM).

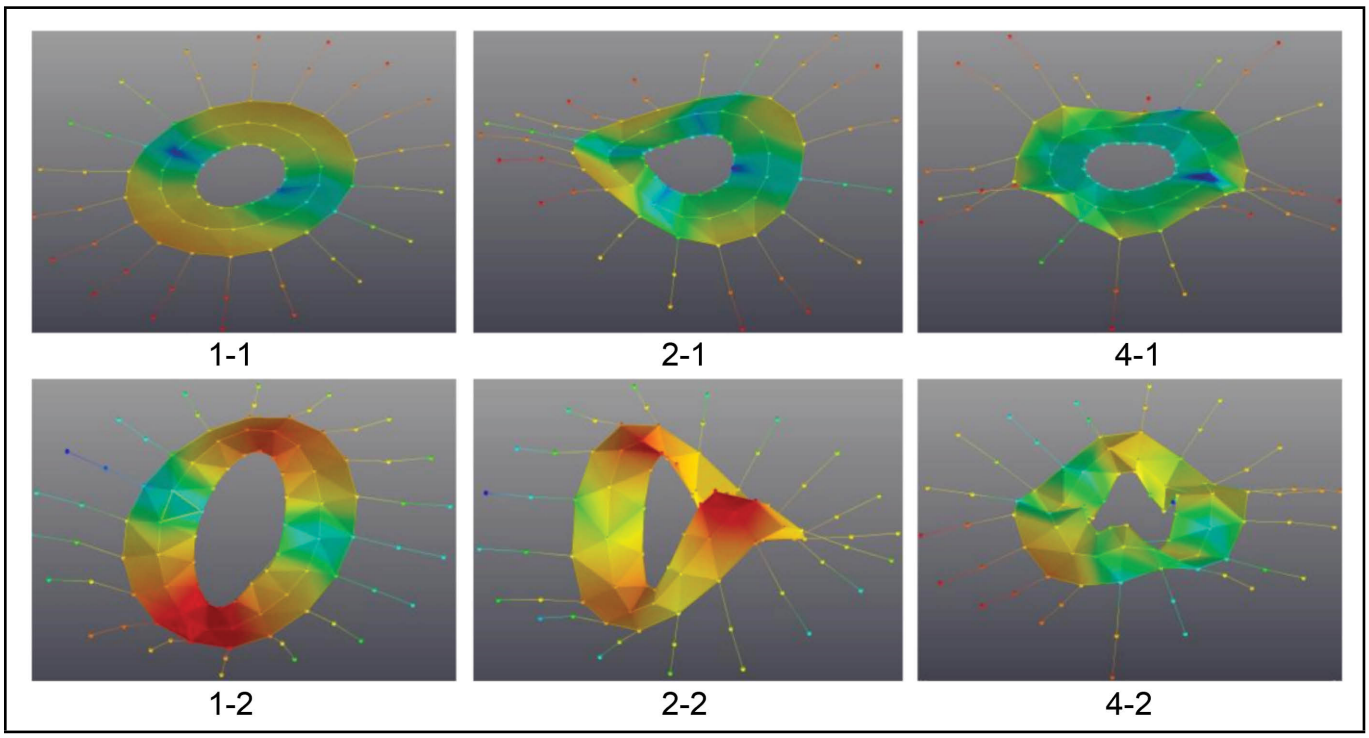

Figure 18. Partial mode shapes of the HC blisks obtained by the experimental testing.